A&A 627, A20 (2019)
https://doi.org/10.1051/0004-6361/201935078

Astronomy & Astrophysics

A population of high-velocity absorption-line systems residing in the Local Group

S. J. D. Bouma, P. Richter, and C. Fechner

Institut für Physik und Astronomie, Universität Potsdam, Karl-Liebknecht-Str. 24/25, 14476 Golm, Germany
e-mail: sbouma@astro.physik.uni-potsdam.de

Received 17 January 2019 / Accepted 22 April 2019

ABSTRACT

Aims. We investigated the ionisation conditions and distances of Galactic high-velocity clouds (HVCs) in the Galactic halo and beyond in the direction of the Local Group (LG) barycentre and anti-barycentre, by studying spectral data of 29 extragalactic background sources obtained with the Cosmic Origins Spectropgraph (COS) installed on the *Hubble* Space Telescope (HST).
Methods. We model column-densities of low, intermediate, and high ions such as Si II, C II, Si III, Si VI, and C IV, and use these data to construct a set of Cloudy ionisation models.
Results. In total, we found 69 high-velocity absorption components along the 29 lines of sight. The components in the direction of the LG barycentre span the entire range of studied velocities, $100 \lesssim |v_{\rm LSR}| \lesssim 400\,{\rm km\,s^{-1}}$, while those in the anti-barycentre sample have velocities up to about $300\,{\rm km\,s^{-1}}$. For 49 components, we infer the gas densities. In the direction of the LG barycentre, the gas densities exhibit a wide range from $\log n_{\rm H} = -3.96$ to -2.55, while in the anti-barycentre direction the densities are systematically higher, $\log n_{\rm H} > -3.25$. The barycentre absorbers can be split into two groups based on their density: a high-density group with $\log n_{\rm H} > -3.54$, which can be affected by the Milky Way radiation field, and a low-density group ($\log n_{\rm H} \leq -3.54$). The latter has very low thermal pressures of $P/k < 7.3\,{\rm K\,cm^{-3}}$.
Conclusions. Our study shows that part of the absorbers in the LG barycentre direction trace gas at very low gas densities and thermal pressures. These properties indicate that the absorbers are located beyond the virial radius of the Milky Way. Our study also confirms results from earlier, single-sightline studies, suggesting the presence of a metal-enriched intragroup medium filling the LG near its barycentre.

Key words. Galaxy: halo – Galaxy: structure – Galaxy: evolution – ISM: kinematics and dynamics – techniques: spectroscopic – ultraviolet: ISM

1. Introduction

Since the first discovery of high-velocity clouds (HVCs) by Muller et al. (1963) in the Milky Way (MW) halo, their origin has been a matter of debate. These HVCs are seen in 21 cm emission or in ultraviolet or optical absorption at radial velocities $|v_{\rm LSR}| > 90{-}100\,{\rm km\,s^{-1}}$. Already more than 50 years ago, Oort (1966) made a list of their possible origins; he suggested that they might be parts of supernova shells, intergalactic gas that is being accreted by the MW, small satellite galaxies of the MW, or independent galaxies of the Local Group (LG). As we know today, most HVCs have low metallicities (<0.3 solar, typically; e.g. Gibson et al. 2000; Wakker 2001; Richter et al. 2001; Collins et al. 2007; Fox et al. 2010; Shull et al. 2011), indicating that they originate from accreted gas, either from satellite galaxies or the intergalactic medium (IGM). The Magellanic Stream (MS), for example, is the result of the gravitational and hydrodynamical interaction between the MW and the Magellanic Clouds (e.g. Putman et al. 1998).

Halo clouds with somewhat lower velocities, namely the intermediate-velocity clouds (IVCs; $40{-}50 < |v_{\rm LSR}| < 90{-}100\,{\rm km\,s^{-1}}$), often appear to be associated with a so-called Galactic fountain. In the Galactic fountain model (Shapiro & Field 1976; Fraternali & Binney 2008), gas is blown out by superbubbles (created by supernova explosions), mixes with the ambient coronal gas, cools, and falls back onto the disc. The relatively high metallicity found in many IVCs (Wakker 2001, and references therein) further supports a Galactic origin of the IVCs as part of the Galactic fountain model. This model, however, does not explain HVCs, thus making it likely that their origin is not within the disc or bulge of the MW (Marasco et al. 2012). Some HVCs may be explained by Galactic rotation, but only when systematic peculiar velocities are assumed. An example is the Outer Arm HVC being an extension of the Outer Arm (Haud 1992).

One of the keys to our understanding of the origin and nature of HVCs is knowing their distances from us. Most HVCs are located within 20 kpc and relatively close to the MW disc (Wakker 2001; Thom et al. 2006, 2008; Wakker et al. 2007, 2008), but some clouds possibly lie outside of the virial radius of the MW (Sembach et al. 2003; Richter et al. 2017). These distant clouds could be evidence that some HVCs have a LG origin. Blitz et al. (1999) proposed that some of the compact HVCs (CHVCs) represent distant (extragalactic) clouds confined by dark matter mini-halos that are moving towards the LG barycentre. This theory has been disputed, however, as stellar components have not been found in these HVCs (Simon & Blitz 2002; Hopp et al. 2003) and the nearby M 31 does not show any significant CHVC population at large galactocentric radii (Westmeier et al. 2008).

In addition to distance, the kinematics of HVCs can also help in understanding their origin. As pointed out by Nicastro et al. (2003), high-velocity O VI absorption in the MW halo has negative velocities for absorbers located between $0° \leq l \leq 180°$, while the systems on the other half of the hemisphere have mostly positive velocities. This trend disappears when velocities

are transformed to the Local Group Standard of Rest (LGSR) frame. Furthermore, using the LGSR or Galactic Standard of Rest (GSR) decreases the amplitude of the average velocity vector of the halo O VI absorption when compared to the LSR. Another, much more detailed study of O VI absorption in the halo (Sembach et al. 2003) confirms that the dispersion around the mean velocity of their absorption systematically decreases if the LSGR or GSR is taken as reference frame. These results indicate that at least one subset of the high-velocity O VI absorbers may not be located in the MW, but rather these absorbers are spatially and kinematically associated with gas filling the LG.

Following up on this, Richter et al. (2017, hereafter R17), in their all-sky HVC absorption survey, compared the absorption velocities of HVCs in the direction of the LG barycentre ($l < 180°$, $b < -30°$) to those of HVCs at $l > 240°$, $b > 60°$ in low and intermediate ions such as Si II and Si III. A velocity dipole is clearly visible: the gas in the direction of the barycentre has negative velocities up to $v_{\rm LSR} = -400\,{\rm km\,s^{-1}}$, while in the opposite direction the velocities are positive up to $v_{\rm LSR} = +300\,{\rm km\,s^{-1}}$. Since such high radial velocities cannot be explained by Galactic rotation, the observed kinematics of the HVC absorber population could be the result of the MW moving towards the LG barycentre and away from the anti-barycentre direction. In this scenario, gas at rest in the LG barycentre or coming from M 31 would have negative velocities as it is coming towards the MW, while LG gas in the anti-barycentre direction would be left behind, leading to positive velocities.

Nearby HVCs are expected to have, on average, lower velocities than those far away; they are also expected to have substantially higher thermal gas pressures as they are located deep within the MW potential well where they are pressure-confined by the ambient hot coronal gas in the outer disc-halo interface. In turn, the very low thermal gas pressures measured in earlier HVC studies in the high-velocity barycentre absorbers towards PKS 2155−304 and Mrk 509 ($P/k < 5\,{\rm K\,cm^{-3}}$; Sembach et al. 1999; Collins et al. 2004) indicate that these clouds cannot reside in the inner halo (as they would collapse rapidly), but are located in the outer Galactic halo or even beyond the MW virial radius in the LG, where the thermal pressures are at least two orders of magnitude lower than in the inner halo (Miller & Bregman 2015; Wolfire et al. 1995).

Finally, an LG origin of barycentre/anti-barycentre high-velocity absorbers is also supported by the ionisation structure of the absorbing gas (as indicated by the column density ratios of low and high ions; see R17) and, in the case of the barycentre clouds, the lack of a two-phase structure of the high-velocity clumps seen in H I 21 cm emission (Winkel et al. 2011).

In this study, we investigate in more detail the physical conditions of the barycentre/anti-barycentre high-velocity absorbers identified in R17 to further explore a possible LG origin of these clouds. To this end, we re-analyse high-velocity absorption along 29 sightlines and model the absorber structure and the ionisation conditions in the gas. Our paper is organised as follows. In Sect. 2 we describe the absorber sample and the analysis methods. In Sect. 3 we present the results of our absorber-modelling analysis. We present the ionisation modelling of the absorbers in Sect. 4. In Sect. 5, we discuss the implications of our results with regard to distance and origin of the absorbers. A summary of our study is given in Sect. 6.

2. Data acquisition and spectral analysis

The 29 active galactic nucleus (AGN) sightlines that are considered in this paper represent a subsample of the 262 sightlines used in the HST/COS Legacy Survey of HVCs presented in R17. For the LG barycentre direction ($l < 180°$, $b < -30°$) our sample includes 19 sightlines; for the LG anti-barycentre direction ($l > 240°$, $b > 60°$) we have 10 sightlines available. Names and Galactic coordinates of the 19 AGNs are given in Table A.1. Their sky distribution, with offsets when one sightline has several absorption components, is shown in Fig. 1.

The original HST/COS data were retrieved from the HST Science Archive at the Canadian Astronomy Data Centre (CADC) and reduced following the strategy described in R17. Most of the COS spectra used here have data from the G130M and G160M gratings, but for ten sightlines only G130M data are available. The COS G130M grating covers a wavelength range of 1150−1450 Å. This range includes the absorption lines of Si II, Si III, Si IV, and C II. Absorption in the important C IV doublet falls into the range of the COS G160M grating, which covers $\lambda = 1405-1775$ Å. The resolving power for both gratings is $R = 16\,000-21\,000$ (Green et al. 2012; Fischer et al. 2018). Table 1 lists wavelengths and oscillator strengths of the transitions used in this study to measure the above-mentioned ions of Si and C. We include Si IV in our analysis here; it is not covered in our progenitor study (R17).

All COS spectra were normalised using the custom-written `span` code (Richter et al. 2011). While in R17 we used the apparent optical depth (AOD) method to measure velocity-integrated column densities for the various metal ions in the high-velocity absorbers, here we model in detail the velocity-component structure of the absorbers using the component-modelling method (Richter et al. 2013). For this, a synthetic spectrum is constructed from a component model for each absorber, so that it matches the observations. For each velocity sub-component of an HVC absorber the component model defines the velocity centroid, the Doppler parameter/b-value, and the column density of the various ions as input parameters. This method is necessary for our purpose as the physical conditions are expected to vary along the individual sub-component. It should be noted that we our aim is to treat each individual absorption sub-component as an individual cloud for which we model the local ionisation conditions. Another advantage of using the modelling approach is that blended lines can be reproduced with a synthetic spectrum, providing additional constraints on the derived column densities and b values.

In this study, we concentrate on HVC absorbers that form the velocity dipole in the LG barycentre and anti-barycentre direction (R17). For the LG barycentre direction region at $l < 180°$, $b < -30°$ we therefore consider only high-velocity absorbers with negative velocities. In the direction of the anti-barycentre at $l > 240°$, $b > 60°$, we consequently only consider HVCs with positive LSR velocities.

In Fig. 2 we show a typical example for our modelling approach for the high-velocity absorbers at $-294\,{\rm km\,s^{-1}}$ and $-223\,{\rm km\,s^{-1}}$ in the direction of the quasar Mrk 1513. All modelling results (component velocities and column densities for each ion) are listed in Table A.1. Further details regarding the modelling method can be found in Richter et al. (2013).

3. Results from the absorption-line analysis

Along the 19 sightlines towards the LG barycentre, 55 high-velocity absorption components with $v_{\rm LSR} \gtrsim -100\,{\rm km\,s^{-1}}$ are identified. One of these components has large uncertainties due to blending and low S/N and therefore is not considered hereafter. All the sightlines in the LG barycentre direction show at

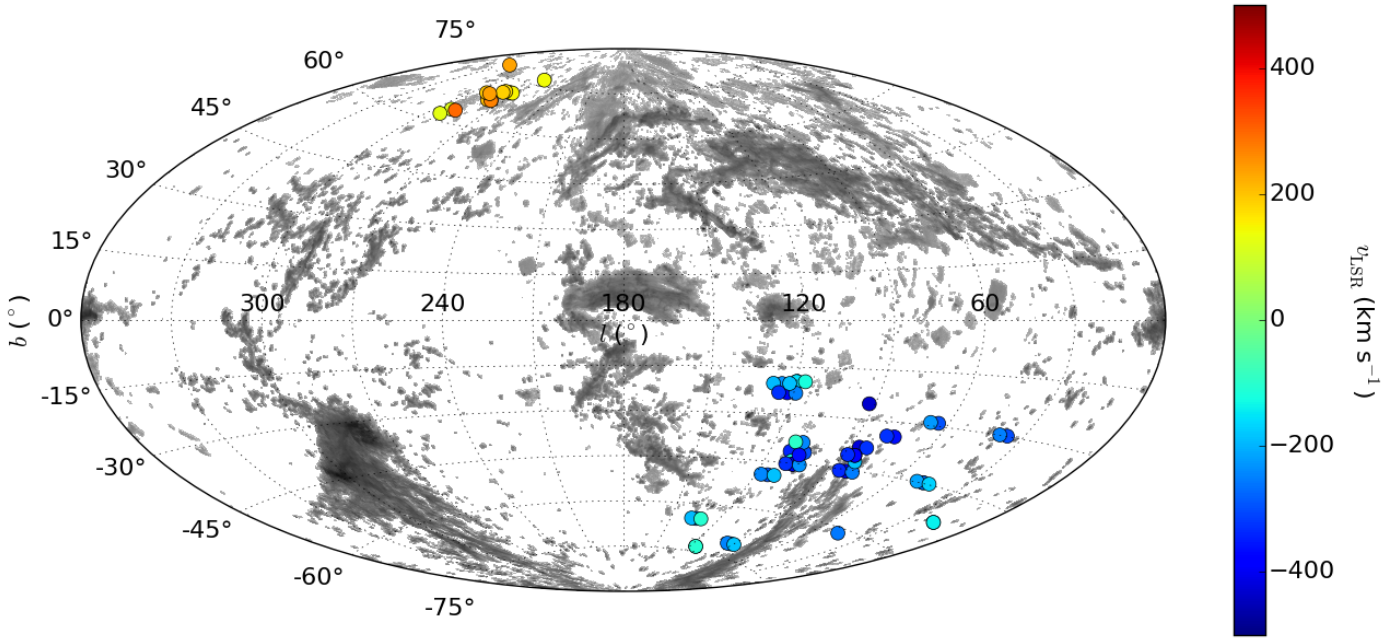

Fig. 1. Sky distribution of the AGN sightlines considered in this study in Galactic coordinates. The colour indicates the observed LSR velocity of the high-velocity components seen in these directions. As can be clearly seen, the high-velocity absorbers form a velocity dipole on the sky along the LG major axis (see R17). H I 21 cm data from Westmeier (2018) is added in greyscale.

Table 1. Atomic data for absorption lines.

Ion	λ_0 (Å)	f
C II	1334.53	0.1284
C IV	1548.20	0.1897
C IV	1550.77	0.0947
Si II	1190.42	0.2919
Si II	1193.29	0.5824
Si II	1260.42	1.1762
Si II	1526.71	0.1328
Si III	1206.50	1.6273
Si IV	1393.76	0.5126
Si IV	1402.77	0.2541

Notes. Data compiled from Morton (2003).

least one high-velocity absorption component, with 17 sightlines having at least two absorption components. Therefore, the observed HVC sky covering fraction in this direction is 100% in our COS sample.

In the anti-barycentre direction, our sample of ten sightlines exhibits 14 individual high-velocity components at $v_{\rm LSR} \geq +100\,{\rm km\,s^{-1}}$. Positive high-velocity absorption is present in all of these sightlines, implying an HVC sky covering fraction of 100% in our data set, with five of the ten sightlines having at least two high-velocity absorption components. The barycentre sightlines show more absorption components (with negative velocities) per sightline than the anti-barycentre sample does for positive velocities.

In Fig. 3, we show the velocity distribution of the 68 high-velocity absorption components in our sample as a histogram. Absorption in the barycentre sample has velocities spanning the entire velocity range used, from $\sim -100\,{\rm km\,s^{-1}}$ down to $-400\,{\rm km\,s^{-1}}$, while the anti-barycentre sample does not have velocities higher than about $+300\,{\rm km\,s^{-1}}$. For both samples, the absorption systems are quite evenly distributed over the velocities, although the barycentre sample has most systems in the bins between $|v_{\rm LSR}| = 200-300\,{\rm km\,s^{-1}}$, which is where the anti-barycentre sample drops off slightly.

In Fig. 4, we compare the column density distribution of the barycentre-absorption components (blue) with the that of the anti-barycentre components (red) for the five different ions considered in our study. The two carbon ions that have been measured, C II and C IV, span a range of slightly higher column densities ($\log N \sim 13-15$) than the three silicon ions Si II, Si III, and Si IV ($\log N \sim 12-14$), owing to the higher cosmic abundance of C. Only 34 of the 51 high-velocity components for which G160M data are available show C IV absorption. Likewise, only 30 of the 67 C II/Si II/Si III HVC components are detected in Si IV. One HVC component is only observed in Si IV and C IV. One explanation for the relatively low detection rate of high ions in this sample and in the all-sky survey (R17) might be that they preferentially arise in low-density environments, for example the diffuse outer layers of 21 cm HVCs, and in diffuse halo structures far away from the Galactic plane (Sembach et al. 1999; Collins et al. 2005).

The ratio of Si II to Si III is shown in Fig. 5. The barycentre sample shows a lower ratio than the anti-barycentre sample, indicating that the gas detected in the barycentre sample is more highly ionised.

4. Ionisation modelling

To obtain more precise information about the physical conditions in the identified high-velocity absorption components we constructed photoionisation models using the Cloudy code version 17.00 (Ferland et al. 2013). For a given ionisation model usually defined by the background ionising radiation field, the absorber geometry, the neutral gas column density, the gas temperature, and the metallicity, Cloudy delivers predictions for the column densities of metal ions as a function of the gas density and ionisation parameter, $U = n_\gamma/n_{\rm H}$. In turn, an observed set of ion column densities in an absorber can be used together with Cloudy

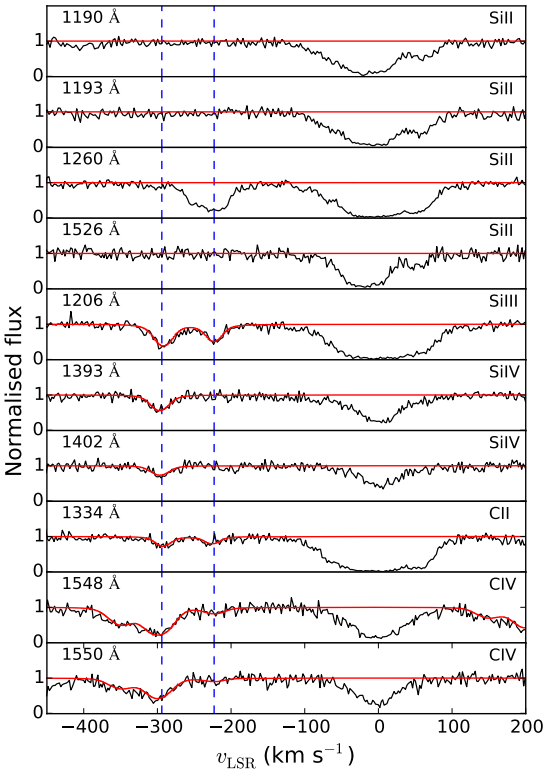

Fig. 2. Example for the simultaneous modelling of high-velocity absorption components in COS spectral data. Shown is spectrum of Mrk 1513 for the various ions considered in our study, plotted in LSR velocity space (black solid line). The synthetic model spectrum (red solid line) accurately reproduces the high-velocity absorption in the 2 high-velocity components at −294 and −223 km s^{-1} seen in this direction, which are indicated with blue dashed lines.

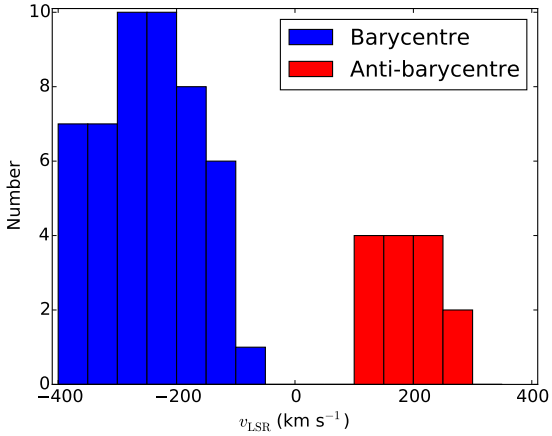

Fig. 3. Velocity distribution of the detected 68 high-velocity absorption components in the LG barycentre/anti-barycentre direction. Absorbers in the barycentre direction are shown in blue and those in the anti-barycentre direction in red.

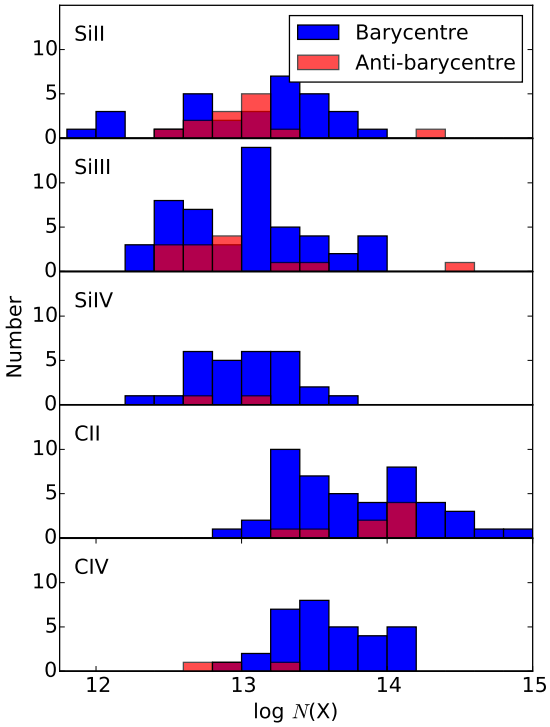

Fig. 4. Column density distribution for measured ions for the LG barycentre and anti-barycentre directions. The barycentre sample is in blue and the anti-barycentre sample in red.

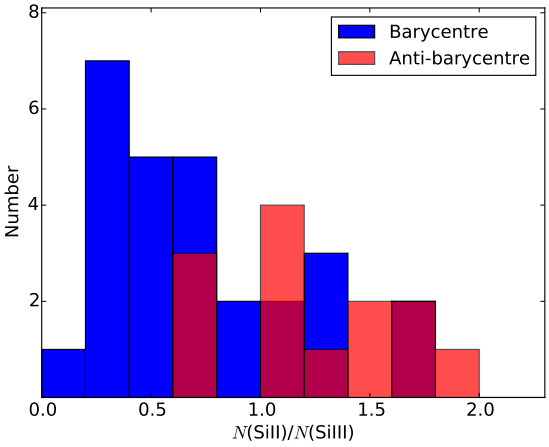

Fig. 5. Ratio of column densities of Si II to Si III for sightlines in the barycentre and anti-barycentre directions.

to constrain the local gas density. In our case the observed ion column densities (or limits) for Si II, Si III, Si IV, C II, and C IV are used to constrain the gas density in the high-velocity absorption components in our sample. A similar strategy was also used in many of our previous HVC absorption studies (e.g. Richter et al. 2009, 2013; Fox et al. 2010, 2013, 2014).

In our grid of Cloudy models, the absorbing clouds are assumed to be plane-parallel slabs illuminated on both sides by the local (z = 0) UV background radiation from Haardt & Madau (2012). For the modelling we do not consider ionising radiation coming from stars in the MW and in M 31, due to the unknown location of the absorbers with respect to their stellar discs. As shown in the MW radiation models by Fox et al. (2005, 2014), the contribution of the local (stellar) radiation field in MW-type galaxies is relevant for CGM absorbers within ∼100 kpc of the plane, and depends on the position of the cloud with respect to the disc. The assumed flux of ionising photons in our Cloudy models therefore represents a lower limit. This needs to be kept in mind when it comes to the interpretation of the derived gas densities and thermal pressures from our models. We will discuss these issues further in Sect. 5.1.3.

The column densities for the above-listed ionisation states are modelled for different ionisation parameters and volume

densities of hydrogen assuming a constant gas temperature of 10 000 K and relative solar abundances as given in Grevesse et al. (2010). A temperature of $\sim 1-2\times10^4$ K is typical for photoionised circumgalactic gas (e.g. Richter et al. 2016), and similar temperatures have been derived in previous studies of individual HVCs in the LG barycentre and anti-barycentre directions (Collins et al. 2005; Sembach et al. 1999). Since we do not have information on the H I column density for most of the absorbers in our sample, we fix the overall metallicity of the gas to a value of $Z_X = 0.1$ to indirectly constrain $\log N(\mathrm{H\,I})$ from the observed ion column densities. A metallicity of $Z_X = 0.1$ is characteristic of many of the most distant HVCs, such as the Magellanic Stream, Complex C, and Complex A (Fox et al. 2013; Richter et al. 2001; Sembach et al. 2004; Wakker et al. 1999).

For some HVCs in our sample, not all elemental abundances fit to the same Cloudy model, suggesting a multiphase-nature of these absorbers. A similar behaviour has also been found in CGM absorbers around other galaxies (see detailed discussion in Richter et al. 2016). More highly ionised species are likely to be found in the outer parts at lower hydrogen volume densities ($\log n_\mathrm{H}$), while the less ionised species are found in the cloud cores at higher $\log n_\mathrm{H}$. However, because not all multiphase clouds necessarily have this (rather oversimplified) internal structure and because Si is also affected by dust depletion effects, our strategy is to fit the Si and C ions independently and then evaluate possible discrepancies with respect to dust depletion and column density errors for each absorber individually. Si IV and C IV are matched together only when Si II, Si III, and C II match the same model at the same $\log n_\mathrm{H}$. For all models, Si III is used as an anchor-ion as it is detected in all but one of the 54 HVCs (and for all HVCs in the anti-barycentre direction). The $\log n_\mathrm{H}$ derived for the one HVC component without Si III is not considered as the more highly ionised Si IV and C IV trace a different gas-phase. For two barycentre HVCs and one anti-barycentre HVC, Si III was the only securely detected ion, making it impossible to obtain $\log n_\mathrm{H}$. For 15 additional HVCs (10 HVCs in the barycentre sample and 5 HVCs in the anti-barycentre direction) we did not find satisfying solutions in our Cloudy models (possibly related to blending and saturation problems), so these absorbers are not considered further in our discussion. In Fig. 6 we show a typical example for our Cloudy modelling approach. A characteristic error of 0.1 dex is assigned to the column densities of the different ions and for $\log n_\mathrm{H}$; this is in agreement with errors found in R17.

For this project, the ionising radiation field of Haardt & Madau (2012) is used. The intensity of this background field is lower than that of the Haardt & Madau (2001) background model and also lower than the value expected from recent measurements of the local H I photoionisation rate (Kollmeier et al. 2014; Wakker et al. 2015; Shull et al. 2015). Generally, a lower intensity of the background field results in higher gas densities. Additionally, the Haardt & Madau (2012) spectrum is harder than the older version, leading to higher metallicities (e.g. Wotta et al. 2019; Chen et al. 2017). To explore the uncertainties related to the scaling and shape of the UV background, as an example we model the absorber towards MR 2251−178 adopting the Haardt & Madau (2001) background, as implemented in Cloudy as Table HM05. The change in the spectral energy distribution of the ionising radiation leads to changes in the column density curves (see Fig. 6). For the HM05 spectrum, the peak of $\log N(\mathrm{Si\,III})$ is closer to the curve of $\log N(\mathrm{C\,II})$. For the MR 2251−178 example system, this results in a density of $\log n_\mathrm{H} = -3.55$ instead of −3.78, thus a 0.23 dex difference. This difference is rather small, although it should be noted that the choice of the ionising radiation field does affect our results to a certain degree.

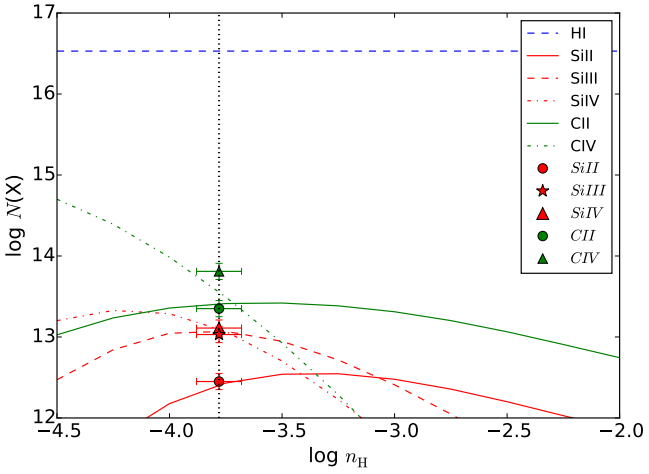

Fig. 6. Cloudy model for the HVC at $v_\mathrm{LSR} = -257\,\mathrm{km\,s^{-1}}$ in the direction of MR 2251−178. Solid, dashed, and dash-dotted lines represent column densities predicted by the Cloudy model for different ions, while the symbols (dots, star, and triangles) show the measured values. This model, with $\log N(\mathrm{H\,I}) = 16.53$, fits Si II, Si III, Si IV, and C II at $\log n_\mathrm{H} = -3.78$, which is indicated by the black dotted line.

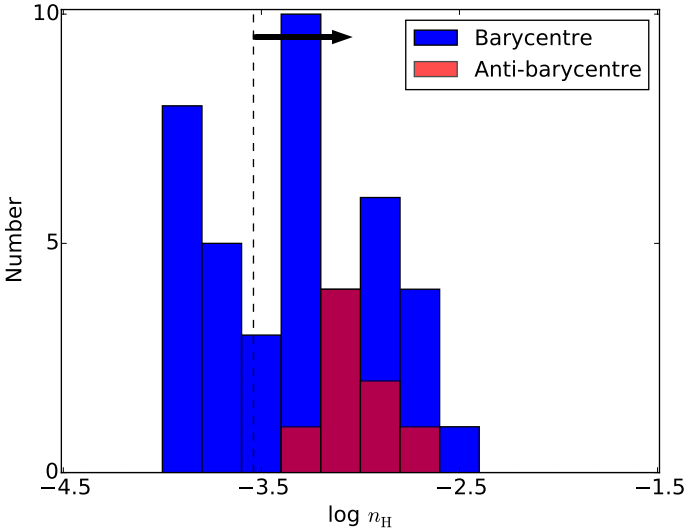

Fig. 7. Histogram of logarithmic hydrogen volume densities for 41 HVCs in the barycentre direction (blue) and 8 HVCs in the anti-barycentre direction (red), based on our Cloudy modelling of these absorbers presented in Sect. 4. The black dashed line and the arrow indicate the region for which the MW radiation field plays a role (see Sect. 5.1.3).

5. Discussion

5.1. Distribution of gas density

In Fig. 7, we show the distribution of the derived logarithmic gas densities, $\log n_\mathrm{H}$, as a histogram. In the barycentre direction (in blue), the densities are spread over a wide range ($\log n_\mathrm{H} = -2.5$ to −4.0), with more than 35% of the absorbers having very low densities $\log n_\mathrm{H} \leq -3.5$. In the anti-barycentre direction the densities are confined to a much narrower range, $\log n_\mathrm{H} = -2.7$ to −3.3.

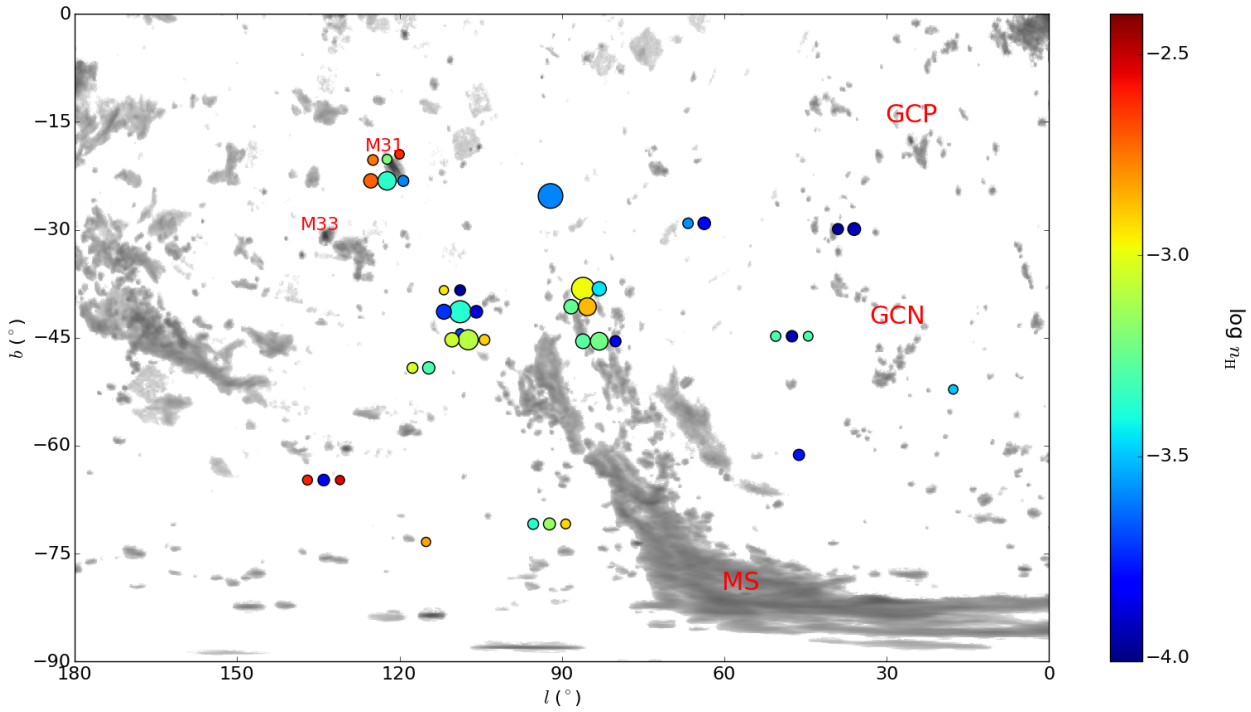

Fig. 8. Sky-distribution of gas densities (see vertical bar at right for colour-coding) for 41 HVCs in the barycentre direction with $\log n_{\rm H}$ measured from Si III, overlaid on the H I map with data from Westmeier (2018), which is based on the LAB survey (Kalberla et al. 2005, 2007). For purposes of display, HVCs along the same sightlines have been given an angular offset. The size of the dots scales with the HVC velocity. Important H I complexes are indicated.

5.1.1. HVCs in the barycentre direction

Figure 8 shows the hydrogen volume densities for HVCs in the barycentre direction plotted on top of the H I 21 cm distribution of high-velocity gas in this region of the sky (grey-shaded areas). There are more HVCs with higher $\log n_{\rm H}$ near the MS and near M 31 than in the direction of the Galactic centre negative (GCN) Complex. Distance estimates for Complex GCN range from 15 to 35 kpc, based on computations of a hypothetical orbit that the clouds composing Complex GCN might follow (Jin 2010). If Complex GCN were connected to the Leading Arm of the Magellanic System, as suggested by simulations from Diaz & Bekki (2011), the distances would be between 14 and 22 kpc. However, Complex GCN might instead be a conglomerate of scattered gas clouds with different origins and distances, as pointed out by Winkel et al. (2011). The absorption properties of the GCN absorbers towards Mrk 509 and PKS 2155−304 (Sembach et al. 1999) indicate extremely low gas pressures of $P/k = 1{-}5\,{\rm cm}^{-3}\,{\rm K}$, inconsistent with gas located in the inner ($d < 50$ kpc) MW halo, but instead pointing towards a LG origin for these gas clouds.

Some of the highest densities are found in the absorbers in the general direction of M 31 (see Fig. 8). These absorbers have relatively low velocities, suggesting that they are close to the MW disc and are not associated with M 31 itself. Absorbers near the tip of the MS show the highest velocities. In this region, the MS has velocities in 21 cm emission between $\sim$−250 and −350 km s^{-1} (Kalberla et al. 2005), demonstrating that, from the kinematics, these clouds could well be associated with the MS. However, the absorber at $(l,b) \sim (110, -40)$ has $v_{\rm LSR} \sim -400\,{\rm km\,s}^{-1}$, indicating that it is not part of the MS. The low densities ($\log n_{\rm H} \sim -3.9$) of some absorbers in this region are also indicative of an extragalactic origin. We will discuss these aspects further in Sect. 5.3, where we include the pressure estimates as additional constraints on the origin of the high-velocity absorbers in the barycentre direction.

5.1.2. HVCs in the anti-barycentre direction

Since in this region there are no prominent clouds seen in the H I 21 cm HVC surveys, we do not provide a density map as for the barycentre direction. The sightlines are all relatively close together on the sky and in velocity (Fig. 1) and the spread in $\log n_{\rm H}$ is much smaller than for the anti-barycentre sample (Fig. 7). This coherency points to a common origin of these high-velocity absorbers as part of a coherent, ionised, high-velocity gas structure located in the inner or outer MW halo.

5.1.3. Role of the Milky Way radiation field

As mentioned above, our ionisation modelling is based on the assumption that the HVC absorbers are only exposed to the extragalactic radiation field at $z = 0$, i.e. any contribution from the MW radiation field has been ignored so far. Since for a given set of input column densities of various metal ions Cloudy delivers the ionisation parameter U as the primary result, there is a degeneracy between the gas density and the intensity of the ionising field in the interpretation of U if Galactic ionising photons are important in addition to the UV background field. This means that the same value for U could be achieved for different combinations of n_γ and $n_{\rm H}$ at different locations inside and outside the MW halo.

Fox et al. (2005, 2014) have modelled in detail the flux of Galactic ionising radiation, demonstrating that the MW radiation field becomes important for galactocentric distances $r \leq 100$ kpc. However, the exact strength of the local radiation field in the MW halo depends strongly on location relative to the Galactic disc. Since we do not know the location (and distance)

of the HVC absorbers in our sample with respect to the disc, the influence of the MW radiation field on the derived HVC gas densities represents a critical aspect in the interpretation of our Cloudy models. To overcome the degeneracy between gas density and photon density we make use of the fact that the gas density in photoionised gas clouds at $T = 10\,000$–$20\,000$ K situated in a galaxy potential well is constrained by the local gas pressure, which is expected to decline rapidly with increasing galactocentric distance. For a fully ionised gas containing 10% helium, the thermal gas pressure P is given by the relation $P/k = 2.3\,n_{\rm H}T$, where k is the Boltzmann constant, $n_{\rm H}$ the hydrogen volume density, and T the temperature of the gas. From the coronal gas model by Miller & Bregman (2015), it follows that $P/k = Cr^{-1.58}$ or $n_{\rm H} = Dr^{-1.58}$, where C and D are constants with values of $C = 3.31 \times 10^4\,{\rm K\,cm^{-1.42}}$, $D = 0.435\,C\,T^{-1}$, and r is the galactocentric distance. By combining the density constraints from the Fox et al. (2006, 2014) radiation field model and the Miller & Bregman (2015) pressure relation, we are able to define a threshold value for U that separates absorbers that are potentially influenced by the Galactic radiation field (thus being located at $r \leq 100$ kpc) from absorbers that must be located at $r > 100$ kpc (i.e. absorbers for which no radiation-field or pressure model solution exists at $r \leq 100$ kpc). Taking the extragalactic radiation field as reference, this threshold for U corresponds to a density threshold of $\log n_{\rm H} = -3.54$.

We conclude that all absorbers, for which our initial Cloudy model delivers gas densities $\log n_{\rm H} \leq -3.54$, must be located beyond $r = 100$ kpc, and thus cannot be significantly influenced by radiation from the MW disc. For all other absorbers with $\log n_{\rm H} > -3.54$, we do not know where they are located in the MW halo. They could be either inside or outside $r = 100$ kpc and therefore the gas densities derived for them from our initial UV background Cloudy model must be regarded as lower limits.

5.2. Density-velocity plane

A correlation is expected between $v_{\rm LSR}$ and $\log n_{\rm H}$ if high velocity and low density are both signs of clouds being at greater distance. In fact, halo clouds are expected to slow down as they get closer to the Galactic disc because the pressure and density of their surrounding medium increases and so does the effect of ram pressure, which scales with $\rho v^2_{\rm infall}$. As a consequence, clouds in the lower halo are expected to have relatively low velocities, while clouds in the outer halo or even beyond can have much higher velocities. Since only the radial component of the space velocity is observed, however, there might be a population of distant clouds that move with high tangential velocities through the outer halo, while we see them as low-velocity HVCs (or even IVCs) because of their small radial velocity component. Clearly, a large sample of MW halo absorbers is required in order to identify possible trends between $v_{\rm LSR}$ and $\log n_{\rm H}$.

It should be noted that the velocities from the HVCs in the direction of M 31 are mostly in the range $-250 \lesssim v_{\rm LSR} \lesssim -120\,{\rm km\,s^{-1}}$, with two HVCs having absolute velocities $>300\,{\rm km\,s^{-1}}$. The systemic velocity of M 31 is about $-300\,{\rm km\,s^{-1}}$ and HVCs with $-300 \lesssim v_{\rm LSR} \lesssim -150\,{\rm km\,s^{-1}}$ might belong to either M 31 or its dwarf companions (Lehner et al. 2015). Thus, some of the HVCs in this direction could be part of the CGM of M 31 instead of that of the MW.

In the upper panel of Fig. 9, we plot $\log n_{\rm H}$ against $v_{\rm LSR}$ for all 49 absorption components. In the lower panel of Fig. 9, we bin the data points in $50\,{\rm km\,s^{-1}}$-wide velocity bins, where we regard the individual densities as fixed values (i.e. in this plot we ignore that densities may represent lower limits).

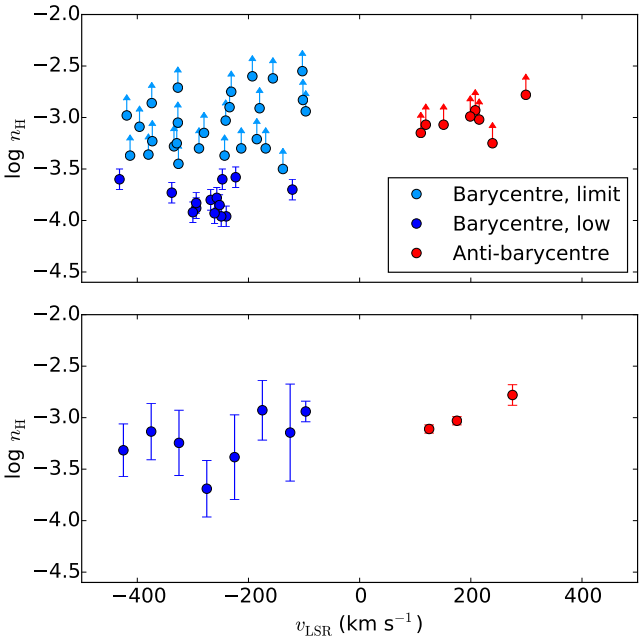

Fig. 9. Volume density of hydrogen plotted against $v_{\rm LSR}$ for our HVC absorber sample. The blue data points show the barycentre absorbers, the red data points indicate the anti-barycentre absorbers. The densities are taken from our Cloudy modelling. *Upper panel*: data points for the 49 HVCs with reliable $n_{\rm H}$ measurements are shown. Lower limits are indicated by light blue symbols and indicated by the arrow. HVCs with $\log n_{\rm H} \leq -3.54$ are shown in dark blue. *Lower panel*: same as above, but data are binned in $50\,{\rm km\,s^{-1}}$-wide velocity bins. For this plot, we regard the individual densities as fixed values (i.e. in this plot we ignore that densities may represent lower limits).

5.2.1. HVCs in the barycentre direction

For the HVCs in the direction of the LG barycentre, the upper panel of Fig. 9 indicates a large scatter in the $v_{\rm LSR}/\log n_{\rm H}$ parameter plane. This trend is expected from the wide range that the barycentre absorbers cover in velocity (Fig. 3) and density (Fig. 7). The sample appears to split into two populations: low-density absorbers with $\log n_{\rm H} \leq -3.54$ that appear to cluster near $v_{\rm LSR} = -300\,{\rm km\,s^{-1}}$, and absorbers with high densities (or density limits) that uniformly scatter in the region $\log n_{\rm H} > -3.54$ and $v_{\rm LSR} = -100$ to $-400\,{\rm km\,s^{-1}}$. The large scatter in $\log n_{\rm H}$ is also reflected in the large error bars seen in the binned version (Fig. 9, lower panel), which indicate the standard deviation for $\log n_{\rm H}$ in each bin. For the barycentre sample, the bin with $v_{\rm LSR} \geq -100\,{\rm km\,s^{-1}}$ has only one HVC, so an error of 0.1 dex is assumed. The same is true for the last bin ($+250 < v_{\rm LSR} < +300\,{\rm km\,s^{-1}}$) in the anti-barycentre sample. Standard deviations in the other two bins in the anti-barycentre sample are smaller than the size of the symbols. Despite the large scatter, the binned version shows a mild trend where the average density increases with decreasing absolute radial velocity. As mentioned above, this behaviour is expected in the scenario where distant clouds move through the MW halo at higher velocities than the nearby clouds, which are slowed down by ram-pressure forces that act predominantly in the inner halo. While this trend is plausible, here we refrain from a deeper discussion to avoid an overinterpretation of the data. The large scatter in $\log n_{\rm H}$ in the overall sample and the fact that for $\log n_{\rm H} \leq -3.54$ our Cloudy modelling provides only lower limits if the Galactic radiation field is taken into account (see Sect. 4) may also be responsible for this trend (at least partly), but the influence

of these effects on the observed $v_{\rm LSR}$/log $n_{\rm H}$ distribution remains unknown.

The Lee statistics (Lee 1979) can be used to determine whether there are indeed two distinct populations in the density distribution of our absorber sample and to provide an estimate for the characteristic density that separates these two populations from each other (separation value). The first step is to split the sample into two subsamples for different values of log $n_{\rm H}$. Next, the second moment of the total population is multiplied by the total number of data points which is then divided by the sum of values derived on either side of the separation value, resulting in the Lee parameter (L). The value of L will be at its maximum for the most likely separation value (see Fitchett & Merritt 1988 for more details). To evaluate L for our absorber sample, all limits on the gas density are regarded as absolute values. The maximum L comes out to 2.45 and is found at a density of log $n_{\rm H} = -3.44$, while the minimum L is 0.09 at log $n_{\rm H} = -2.44$. The split at log $n_{\rm H} = -3.44$ is marginally higher than the value derived above (-3.54), resulting in two more absorbers being assigned to the low-density subsample. Overall, however, the results from the Lee statistics agree very well with the results based on the estimated influence of the Galactic radiation field (Sect. 5.1.3).

Despite the uncertainties in modelled densities, the existence of a distinct population of barycentre absorbers with log $n_{\rm H} \leq -3.54$ and $v_{\rm LSR} \leq -120\,{\rm km\,s^{-1}}$ is securely constrained by the distribution shown in Fig. 9 and further strengthened by the Lee statistics. These results point toward photoionised halo absorbers with very low gas pressures (see discussion in Sect. 5.3).

5.2.2. HVCs in the anti-barycentre direction

For the HVCs in the anti-barycentre direction, all absorbers cluster in the density-velocity plane in the region $v_{\rm LSR} \sim +300\,{\rm km\,s^{-1}}$ and log $n_{\rm H} \sim -3.0$ with very little scatter (Fig. 9, upper and lower panel). Thus, the anti-barycentre absorbers have on average significantly higher densities and lower absolute radial velocities than the barycentre absorbers. This striking asymmetry between barycentre and anti-barycentre HVCs has also been discussed in R17.

It should be noted that the anti-barycentre sample contains only eight absorbers with well-constrained gas densities, compared to the 41 absorbers in the barycentre sample. Only ~35% of the barycentre absorbers have low log $n_{\rm H} < -3.54$.

If the anti-barycentre sample had the same fraction of low-density clouds as the barycentre sample (~35% having log $n_{\rm H} < -3.54$), we would expect to find only three of these systems in the anti-barycentre direction at this sample size. Because of the low number statistics, we could have missed low-density absorbers in the anti-barycentre direction that are not covered by our sample.

5.3. Gas pressures and galactocentric distances

High-velocity clouds are expected to be in pressure equilibrium with their environment, or else they would not exist very long. Since the coronal gas pressure in the inner Galactic halo ($r < 50$ kpc) is expected to be $P/k \gtrsim 100\,{\rm K\,cm^{-3}}$ (Wolfire et al. 1995; Miller & Bregman 2015), HVCs in the inner Galactic halo should have similar pressures. Here we assumed a constant temperature of 10 000 K for the photoionised HVCs. For the errors in the pressure estimates we allowed the temperature to vary in the range $T = 5000-20\,000$ K and also considered the individual errors derived for the densities from the Cloudy modelling.

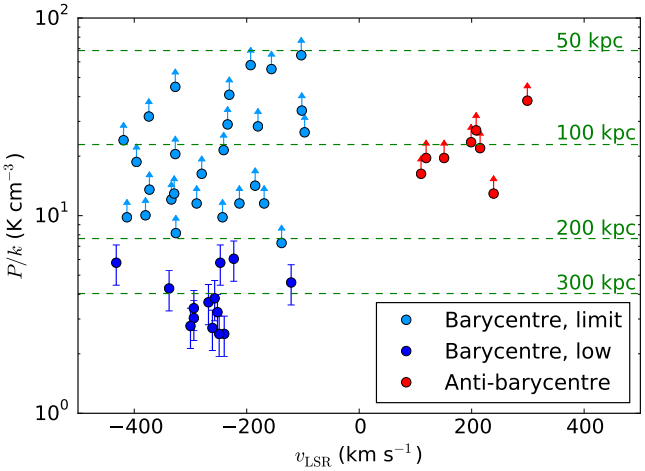

Fig. 10. Same as Fig. 9, but now with the pressure values, log P/k, on the y-axis. Lower pressure limits are indicated by the arrows (see also Sect. 5.2.1). The dashed green lines show distance-scale based on the halo pressure model from Miller & Bregman (2015).

Looking at the range of hydrogen densities (or limits) derived for the barycentre and anti-barycentre sample, all HVCs have pressure values (or lower limits) in the range $P/k \sim 2.5-50\,{\rm K\,cm^{-3}}$, as indicated in Fig. 10. For the 41 absorbers in the barycentre direction, for which absolute values of log $n_{\rm H}$ could be determined (see Sect. 5.1.1), we derived gas pressures in the range $P/k \sim 2.5-10\,{\rm K\,cm^{-3}}$, which is far lower than expected for the inner halo. The lowest pressures were found for the HVCs in the direction of Complex GCN and the HVCs that are (in projection) close to the tip of the MS.

Figure 10 shows $v_{\rm LSR}$ plotted against P/k together with a distance scale (dashed green lines), based on the pressure-distance relation described in Miller & Bregman (2015, see their Sect. 5.4). Applying their model to our data, we calculated for each absorber the galactocentric distance (or limit) that corresponds to the derived pressure (or limit). As can be seen, the distances derived for the low-density barycentre HVCs with log $n_{\rm H} \leq -3.54$ are very large, $r > 200$ kpc, thus beyond the assumed virial radius of the MW.

It should be noted that the Miller & Bregman (2015) pressure model considers only the MW gravitational potential, but not the LG potential, which defines the pressure floor for any gas absorber located inside the LG. The pressure was estimated to decrease from $P/k \sim 10\,{\rm K\,cm^{-3}}$, at a distance of 200 kpc from the MW centre, to $P/k \sim 0.1\,{\rm K\,cm^{-3}}$ in the LG intra-group medium in the direction of M 31 (Nuza et al. 2014; Richter et al. 2017). Therefore, the lowest pressure values derived from our sample correspond to gas outside of the MW's virial radius possibly residing in the LG's intra-group medium.

The low pressures derived here can be compared to CGM clouds within the virial radius of other more distant galaxies. Gas pressures of clouds in the CGM of low-redshift galaxies have been estimated by Werk et al. (2014) and Stocke et al. (2013), indicating $P/k \sim 3-100\,{\rm K\,cm^{-3}}$ within the virial radius. Thus, the lowest pressures in our HVC sample fall just below the range suggested for CGM gas in the local Universe.

From our pressure modelling we conclude that all barycentre HVC absorbers with gas densities lower than log $n_{\rm H} = -3.54$ (14 absorbers) and that are predominantly associated with Complex GCN and the outer boundary of the MS, are most likely located beyond the MW's virial radius in the LG. For the other remaining barycentre and anti-barycentre absorbers with

$\log n_{\rm H} > -3.54$ (35 absorbers) the derived density and pressure limits do not provide constraints on the location of these absorbers inside or outside the MW halo.

The barycentre HVCs near Complex GCN and the tip of the MS represent a distinct population of high-velocity absorbers that are peculiar in other properties as well. As discussed in R17, the region near Complex GCN and the tip of the MS contains very little H I 21 cm emission, but is very pronounced in O VI absorption (Sembach et al. 2003; Wakker et al. 2003). In addition, the many scattered 21 cm clumps do not show the typical two-phase characteristics of nearby HVCs with cold cloud cores and extended diffuse gas layers, indicating that they reside in a very low-density environment.

With only the 14 barycentre absorbers having distinct properties that point to a LG origin, our study does not provide further evidence for the scenario where the observed velocity dipole of HVC absorbers in the barycentre and anti-barycentre absorbers is a result of the overall motion of the MW with respect to the LG's intragroup medium (R17). Since the distances found in our study are derived from the gas densities and pressures, they depend on the background radiation field and the assumed MW halo model, among other assumptions. The low number statistics for the anti-barycentre sample adds to these uncertainties. However, our study also does not exclude such a model and the observed large negative velocities of the LG absorbers in the barycentre direction may well be related to the MW's overall motion towards M 31 and its companions (see also Nuza et al. 2014).

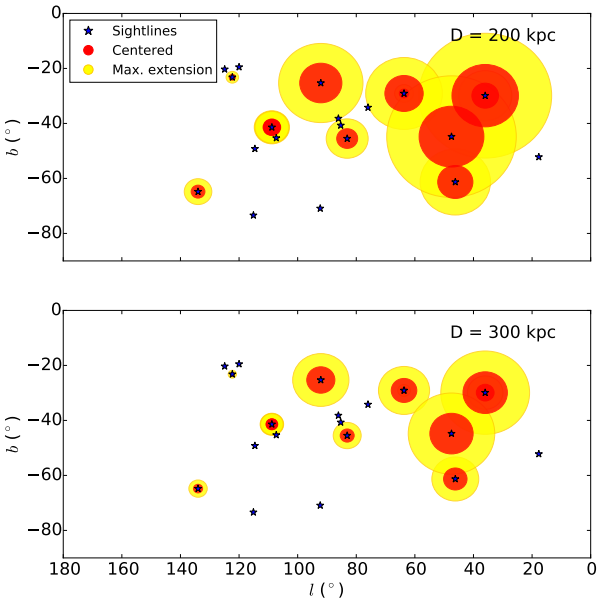

Fig. 11. Positions and angular sizes on the sky of the absorbers with $\log n_{\rm H} \leq -3.54$ in the direction of the LG barycentre. For sightlines with multiple low-density absorbers, the one with the largest angular size has been plotted. Red filled circles indicate the size if the cloud were centred on the sightline along which it is detected. Yellow circles instead indicate the maximum extent of the cloud assuming that the AGN sightline passes the edge of the cloud.

5.4. Masses and sizes of the HVCs

The sizes and masses of the absorbers can be estimated from $\log N$(H) and $\log n_{\rm H}$, based on the values derived from the Cloudy models. We note that a direct measurement of $\log N$(H I) from Lyα absorption is not possible as Galactic disc emission and absorption dominates the Lyα spectrum up to about 400 km s^{-1}. Here we computed sizes and masses for the subsample of barycentre clouds with $\log n_{\rm H} \leq -3.54$ by using the Cloudy results in combination with Eqs. (6)–(8) presented in Richter et al. (2009). From this we derived linear diameters between 5 and 39 kpc; instead, the masses range from $\sim 10^5$ to $10^8\,M_\odot$ for the most massive cloud, with the median mass being $4.0 \times 10^6\,M_\odot$. The angular sizes of the absorbers on the sky depend on their distances. Assuming a distance of 200 kpc, the estimated angular sizes are up to 11°. Assuming instead that the absorbers are located at 300 kpc reduces their angular sizes by a factor of 2/3. Figure 11 displays the location of the barycentre absorbers on the sky together with their angular sizes.

If we further assume that the absorbers are centred on the AGN sightline along which they are observed, none of the absorbers are expected to cover multiple AGN sightlines. This is true for both 200 kpc and 300 kpc distances, although there are two systems near the tip of the MS where the estimated extent of the clouds almost overlaps with other AGN sightlines. Since these other sightlines do not show low-density absorption, we conclude that these clouds cannot be at distances closer than 200 kpc as they would be picked up by multiple AGN sightlines. This conclusion depends, however, on various assumptions, for instance the assumed spherical geometry of the clouds.

If the absorbers are not centred on the sightline along which which they are detected, there are several cases where clouds may cover multiple sightlines. However, only in the case of the four absorbers in the direction of Complex GCN (see also Fig. 8) do the different sightlines all show coherent low-density absorption that could be associated with overlapping absorbers. As seen in Fig. 8, these possibly overlapping absorbers in the direction of the Complex GCN all have similar velocities and similar densities. If this is indeed one and the same low-density cloud stretching over multiple AGN sightlines, a distance of about 200 kpc is needed since there is no more overlap at 300 kpc. However, a conglomerate of small clouds with similar properties could also mimic such an absorption pattern. This would fit the picture of the H I gas in this region, as seen in Fig. 8.

In conclusion, the estimated masses and sizes do not provide any additional firm constraints on the distance and origin of the barycentre absorbers, but they are fully in line with a LG origin of these clouds, as concluded from the low gas pressures.

6. Summary and conclusions

In this paper, 68 high-velocity absorption systems in a sample of 29 HST/COS spectra were studied to learn more about the origin of these HVCs and their relation to the intragroup medium of the LG. Of these spectra, 19 are in the direction of the LG barycentre and 10 are in the LG anti-barycentre direction. The velocity range studied for the barycentre sample is $-100 < v_{\rm LSR} < -400$ km s^{-1}, while that for the anti-barycentre sample is $+100 < v_{\rm LSR} < +400$ km s^{-1}. We measured column densities for the ions Si II, Si III, Si IV, C II, and C IV in these absorbers by modelling in detail the absorption patterns with synthetic spectra. These column densities were then used together with Cloudy to model the ionisation conditions in the absorbers and to determine the local gas densities, $\log n_{\rm H}$.

The density constraints that we derived from this modelling indicate that the absorbers span a wide range in gas densities from $\log n_{\rm H} = -2.5$ to -4.0. The positive-velocity absorbers all have $\log n_{\rm H} > -3.3$, corresponding to thermal pressures of

$P/k > 11.5\,\mathrm{K\,cm^{-3}}$ for $T = 10\,000\,\mathrm{K}$. These absorbers must be located within $R_{\mathrm{vir}} = 200\,\mathrm{kpc}$ of the MW in the inner and outer halo. The negative-velocity absorbers are split into two different populations. One population (27 systems) has $\log n_{\mathrm{H}} > -3.54$ and $P/k > 7.3\,\mathrm{K\,cm^{-3}}$, thus similar to the positive-velocity absorbers, indicating a location within R_{vir}. The other population (14 systems) consists of absorbers with very low gas densities ($\log n_{\mathrm{H}} \leq -3.54$) and very low thermal pressures ($P/k < 7.3\,\mathrm{K\,cm^{-3}}$), suggesting that these absorbers trace gas situated outside the MW halo in the LG intragroup medium. The derived gas densities and pressures depend on several assumptions, such as the ionising radiation field. Therefore, the derived distances of the absorbers conservatively should be regarded as approximate values. The low-density, low-pressure absorbers appear to be spatially and kinematically connected to HVC Complex GCN and the tip of the Magellanic Stream, but also could lie behind these complexes. A LG origin for these absorbers is further supported by other observed peculiarities, such as the lack of a pronounced core-envelope structure (Winkel et al. 2011) and the excess of O VI absorption (Sembach et al. 2003).

To more precisely pinpoint the exact location of the (predominantly ionised) low-density LG absorbers beyond the virial radius of the MW using the bracketing method (e.g. Wakker et al. 2007, 2008; Richter et al. 2015), combined spectroscopic observations of the most distant globular clusters and adjacent AGN sightlines are necessary. While the bracketing method can be used for nearby clouds using bright halo stars and AGNs (e.g. Peek 2018), this is not possible for distances near or outside the virial radius. The strategy of using distant globular clusters has to wait for future UV instrumentation, however, as the eligible background sources are too faint to be observed with HST/COS at realistic integration times.

Acknowledgements. We would like to thank the referee for the very useful comments and suggestions.

References

Blitz, L., Spergel, D. N., Teuben, P. J., Hartmann, D., & Burton, W. B. 1999, ApJ, 514, 818
Chen, H.-W., Johnson, S. D., Zahedy, F. S., Rauch, M., & Mulchaey, J. S. 2017, ApJ, 842, L19
Collins, J. A., Shull, J. M., & Giroux, M. L. 2004, ApJ, 605, 216
Collins, J. A., Shull, J. M., & Giroux, M. L. 2005, ApJ, 623, 196
Collins, J. A., Shull, J. M., & Giroux, M. L. 2007, ApJ, 657, 271
Diaz, J., & Bekki, K. 2011, MNRAS, 413, 2015
Ferland, G. J., Porter, R. L., van Hoof, P. A. M., et al. 2013, Rev. Mex. Astron. Astrofis., 49, 137
Fischer, W. J., et al. 2018, Cosmic Origins Spectrograph Instrument Handbook, Version 10.0 (Baltimore: STScI)
Fitchett, M., & Merritt, D. 1988, ApJ, 335, 18
Fox, A. J., Wakker, B. P., Savage, B. D., et al. 2005, ApJ, 630, 332
Fox, A. J., Savage, B. D., & Wakker, B. P. 2006, ApJS, 165, 229
Fox, A. J., Wakker, B. P., Smoker, J. V., et al. 2010, ApJ, 718, 1046
Fox, A. J., Richter, P., Wakker, B. P., et al. 2013, ApJ, 772, 110
Fox, A. J., Wakker, B. P., Barger, K. A., et al. 2014, ApJ, 787, 147
Fraternali, F., & Binney, J. J. 2008, MNRAS, 386, 935
Gibson, B. K., Giroux, M. L., Penton, S. V., et al. 2000, AJ, 120, 1830
Green, J. C., Froning, C. S., Osterman, S., et al. 2012, ApJ, 744, 60
Grevesse, N., Asplund, M., Sauval, A. J., & Scott, P. 2010, Ap&SS, 328, 179
Haardt, F., & Madau, P. 2001, in Clusters of Galaxies and the High Redshift Universe Observed in X-rays, eds. D. M. Neumann, & J. T. V. Tran, 64
Haardt, F., & Madau, P. 2012, ApJ, 746, 125
Haud, U. 1992, MNRAS, 257, 707
Hopp, U., Schulte-Ladbeck, R. E., & Kerp, J. 2003, MNRAS, 339, 33
Jin, S. 2010, MNRAS, 408, L85
Kalberla, P. M. W., Burton, W. B., Hartmann, D., et al. 2005, A&A, 440, 775
Kalberla, P. M. W., Dedes, L., Kerp, J., & Haud, U. 2007, A&A, 469, 511
Kollmeier, J. A., Weinberg, D. H., Oppenheimer, B. D., et al. 2014, ApJ, 789, L32
Lee, K. L. 1979, J. Am. Stat. Assoc., 74, 708
Lehner, N., Howk, J. C., & Wakker, B. P. 2015, ApJ, 804, 79
Marasco, A., Fraternali, F., & Binney, J. J. 2012, MNRAS, 419, 1107
Miller, M. J., & Bregman, J. N. 2015, ApJ, 800, 14
Morton, D. C. 2003, ApJS, 149, 205
Muller, C. A., Oort, J. H., & Raimond, E. 1963, Académie des Sciences Paris Comptes Rendus, 257, 1661
Nicastro, F., Zezas, A., Elvis, M., et al. 2003, Nature, 421, 719
Nuza, S. E., Parisi, F., Scannapieco, C., et al. 2014, MNRAS, 441, 2593
Oort, J. H. 1966, Bull. Astron. Inst. Neth., 18, 421
Peek, J. 2018, QuaStar: The First Unobscured View of the Milky Way's Circumgalactic Medium, HST Cycle 26 Abstract Catalog
Putman, M. E., Gibson, B. K., Staveley-Smith, L., et al. 1998, Nature, 394, 752
Richter, P., Sembach, K. R., Wakker, B. P., et al. 2001, ApJ, 559, 318
Richter, P., Charlton, J. C., Fangano, A. P. M., Bekhti, N. B., & Masiero, J. R. 2009, ApJ, 695, 1631
Richter, P., Krause, F., Fechner, C., Charlton, J. C., & Murphy, M. T. 2011, A&A, 528, A12
Richter, P., Fox, A. J., Wakker, B. P., et al. 2013, ApJ, 772, 111
Richter, P., de Boer, K. S., Werner, K., & Rauch, T. 2015, A&A, 584, L6
Richter, P., Wakker, B. P., Fechner, C., et al. 2016, A&A, 590, A68
Richter, P., Nuza, S. E., Fox, A. J., et al. 2017, A&A, 607, A48
Sembach, K. R., Savage, B. D., Lu, L., & Murphy, E. M. 1999, ApJ, 515, 108
Sembach, K. R., Wakker, B. P., Savage, B. D., et al. 2003, ApJS, 146, 165
Sembach, K. R., Wakker, B. P., Tripp, T. M., et al. 2004, ApJS, 150, 387
Shapiro, P. R., & Field, G. B. 1976, ApJ, 205, 762
Shull, J. M., Stevans, M., Danforth, C., et al. 2011, ApJ, 739, 105
Shull, J. M., Moloney, J., Danforth, C. W., & Tilton, E. M. 2015, ApJ, 811, 3
Simon, J. D., & Blitz, L. 2002, ApJ, 574, 726
Stocke, J. T., Keeney, B. A., Danforth, C. W., et al. 2013, ApJ, 763, 148
Thom, C., Putman, M. E., Gibson, B. K., et al. 2006, ApJ, 638, L97
Thom, C., Peek, J. E. G., Putman, M. E., et al. 2008, ApJ, 684, 364
Wakker, B. P. 2001, ApJS, 136, 463
Wakker, B. P., Howk, J. C., Savage, B. D., et al. 1999, Nature, 402, 388
Wakker, B. P., Savage, B. D., Sembach, K. R., et al. 2003, ApJS, 146, 1
Wakker, B. P., York, D. G., Howk, J. C., et al. 2007, ApJ, 670, L113
Wakker, B. P., York, D. G., Wilhelm, R., et al. 2008, ApJ, 672, 298
Wakker, B. P., Hernandez, A. K., French, D. M., et al. 2015, ApJ, 814, 40
Werk, J. K., Prochaska, J. X., Tumlinson, J., et al. 2014, ApJ, 792, 8
Westmeier, T. 2018, MNRAS, 474, 289
Westmeier, T., Brüns, C., & Kerp, J. 2008, MNRAS, 390, 1691
Winkel, B., Ben Bekhti, N., Darmstädter, V., et al. 2011, A&A, 533, A105
Wolfire, M. G., McKee, C. F., Hollenbach, D., & Tielens, A. G. G. M. 1995, ApJ, 453, 673
Wotta, C. B., Lehner, N., Howk, J. C., et al. 2019, ApJ, 872, 81

Appendix A: Chemical abundances

Table A.1. Chemical abundances.

AGN name	l (°)	b (°)	$v_{\rm LSR}$ (km s^{-1})	log N(Si II)	log N(Si III)	log N(Si IV)	log N(C II)	log N(C IV)	log $n_{\rm H}$
2MASX-J01013113+4229356	124.9	−20.3	−231	13.71	13.40	13.21	14.59	13.50	−2.75
			−193	13.24	12.69	13.04	14.52	13.90	−3.80
AKN-564	92.1	−25.3	−432	12.79	13.39	13.21	13.90	13.40	−3.60
HS-0033+4300	120.0	−19.5	−202	...	13.15	13.18	14.03	13.98	−3.40
			−156	13.32	12.85	...	14.25	13.20	−2.62
			−119	13.78	13.05	...	14.86	...	−2.30
LBQS-0107−0235	134.0	−64.8	−268	...	12.63	12.67	13.20	13.65	−3.80
			−193	13.02	12.56	...	13.27	13.00	−2.60
			−103	13.14	12.66	...	13.76	13.44	−2.55
MR2251−178	46.2	−61.3	−257	12.45	13.03	13.11	13.35	13.81	−3.78
MRK335	108.8	−41.4	−413	12.18	12.49	...	13.32	...	−3.37
			−338	12.19	12.80	...	13.34	13.28	−3.73
			−294	...	12.58	...	...	13.29	−3.88
			−240	...	12.37	...	...	13.27	−3.96
			−121	11.98	12.54	...	13.50	...	−3.70
			−97	13.28	13.18	...	14.16	...	−2.94
MRK-509	36.0	−29.9	−300	12.15	13.20	13.10	13.58	14.07	−3.92
			−249	...	12.56	...	12.93	13.49	−3.96
MRK1513	63.7	−29.1	−294	...	13.01	13.09	13.39	14.02	−3.83
			−223	...	12.76	...	13.22	12.98	−3.58
NGC 7469	83.1	−45.5	−373	13.04	13.20	12.66	13.97	...	−3.23
			−334	13.45	13.62	13.21	14.12	...	−3.28
			−252	...	12.70	12.80	13.23	...	−3.85
			−185	...	12.40	12.85	13.12	...	−4.18
PG0003+158	107.3	−45.3	−431	...	12.40	13.06	13.12	...	−4.40
			−396	12.76	12.78	...	13.70	13.35	−3.09
			−327	13.25	13.19	...	14.10	...	−3.05
			−234	...	12.53	...	13.53	13.39	−2.90
			−360	...	...	12.78	...	13.76	−4.18 [1]
PHL1811	47.5	−44.8	−358	...	12.61	12.67	...	13.78	−3.80
			−261	...	13.03	12.57	13.31	13.47	−3.93
			−213	13.70	13.94	12.88	14.38	...	−3.30
			−169	12.90	13.12	13.43	13.76	14.10	−3.30
PKS2155−304	17.7	−52.2	−275	...	12.22	...	...	13.56 [2]	−4.15
			−138	12.73	13.18	12.62	13.78	13.48 [2]	− 3.50
Q2251+155	86.1	−38.2	−419	13.98	13.90	13.28	14.56	...	−2.98
			−372 [3]	13.90 [3]	14.53 [3]	14.38 [3]	14.78 [3]	13.79 [3]	−3.68 [3]
			−326	13.54	13.90	13.65	14.49	13.74	−3.45
QSO0045+3926	122.3	−23.2	−380	12.86	13.14	...	14.15	13.12	−3.36
			−327	...	12.26	...	13.46	...	−2.71
			−246	12.78	13.36	13.14	13.87	14.02	−3.60
			−185	13.50	13.68	12.83	14.70	13.57	−3.21
QSO-B0026+129	114.6	−49.2	−187	...	12.46	...	...	...	−3.30
			−289	...	12.81	12.30	13.45	...	−3.03
			−241	12.78	12.73	...	13.54	...	−2.85
QSO-B2214+139	76.0	−34.2	−360	...	13.22	12.65	13.42	...	−3.18
			−327	...	13.01	...	13.26	...	−3.95
SDSSJ001224.01−102226.5	92.3	−70.9	−280	13.44	13.53	12.81	14.35	...	−3.15
			−243	13.22	13.53	13.48	13.96	14.17	−3.37
			−180	13.40	13.27	...	14.17	13.33	−2.91
SDSSJ004222.29−103743.8	115.1	−73.4	−147	...	12.82	...	...	...	−2.85
			−102	13.32	13.10	...	14.09	13.40	−2.83

Notes. [1]log $n_{\rm H}$ from Si IV and C IV. [2]From Collins et al. (2004). [3]No reliable measurement due to blending and low S/N.

Table A.1. continued.

AGN name	l (°)	b (°)	$v_{\rm LSR}$ (km s^{-1})	log N(Si II)	log N(Si III)	log N(Si IV)	log N(C II)	log N(C IV)	log $n_{\rm H}$
SDSSJ225738.20+134045.4	85.3	−40.7	−421	...	13.00	...	13.70	...	−3.17
			−374	13.72	13.48	13.37	14.25	13.79	−2.86
			−329	13.33	13.48	13.25	14.17	13.80	−3.25
RXJ1230	291.3	63.7	119	12.68	12.68	...	13.88	12.83	−3.07
			299	13.06	12.77	...	14.01	12.77	−2.78
SDSSJ121640	278.9	68.4	215	12.58	12.55	...	...	...	−3.02
SDSSJ121850	276.9	71.5	110	13.14	13.25	...	14.05	...	−3.15
			151	12.94	12.93	...	14.10	...	−3.07
SDSSJ122018	281.6	68.3	208	13.00	12.85	13.10	...	...	−2.93
			273	12.87	12.72	...	...	...	−2.91
SDSSJ122102	269.2	76.8	143	13.38	13.52	...	14.15	...	−3.20
SDSSJ122312	280.5	71.5	172	13.10	12.85	...	13.80	...	−2.82
SDSSJ122317	281.1	71.1	188	12.80	12.58	...	13.59	...	−2.84
SDSSJ123304	293.1	62.0	125	12.71	12.59	12.68	13.35	13.30	−2.96
SDSSJ123426	290.6	69.9	199	13.00	12.95	...	...	...	−2.99
			239	14.34	14.50	...	...	...	−3.25
VV2006J131545	329.9	77.0	238	...	12.93	...	...	...	−2.68